Nanometric three-dimensional tracking of individual quantum dots in cells

Laurent Holtzer, Tobias Meckel, and Thomas Schmidt[a)]

Physics of Life Processes, Leiden Institute of Physics, Leiden University, 2333 CA Leiden, The Netherlands

Wide-field single-molecule fluorescence microscopy has become an established tool for the study of dynamic biological processes which occur in the plane of a cellular membrane. In the current study we have extended this technique to the three-dimensional analysis of molecular mobility. Introduction of a cylindrical lens into the emission path of a microscope produced some astigmatism which was used to obtain the full three-dimensional position information. The localization accuracy of fluorescent objects was calculated theoretically and subsequently confirmed by simulations and by experiments. For further validation individual quantum dots were followed when passively diffusing and actively transported within life cells. © *2007 American Institute of Physics*. [DOI: 10.1063/1.2437066]

Wide-field single-molecule fluorescence microscopy has become an established experimental technique in the biosciences. So far its strength has mainly been exploited in two-dimensional (2D) systems: for the observation of individual molecules immobilized to substrates, and for the tracking of individual proteins in the cellular membranes.[1–4] The latter is typically carried out at video rate allowing for simultaneous tracking of several molecules with very high lateral accuracy, far below the diffraction limit.[5] An extension of that technology to a full three-dimensional (3D) single-molecule imaging and tracking platform is highly desirable given that most biological processes take place in the 3D environment of the cell. Several methods to acquire information on the third dimension have been recently developed, i.e., using image stacks,[6,7] off-focus imaging,[8] or by orbiting a focused laser beam around a particle.[9] While all these methods have shown to yield valuable information, the main disadvantage is either the imaging speed (only slow molecules can be followed) or the ability to image only one or a few molecules at a time.

Here we describe a simple one-camera 3D wide-field fluorescence setup which can image a large area (50 μm)^2 at high frame rates (~25 Hz). The setup was adapted from a previously described 2D wide-field single-molecule fluorescence setup.[10] By adding a cylindrical lens (f=10 m) into the detection path of the setup, unambiguous information on the 3D position of individual objects far beyond the diffraction limit was obtained. Our detection scheme follows an earlier development on tracking fluorescing 100 nm beads on a time scale of 0.5 s (Ref. 11) but with higher sensitivity and higher time resolution. The setup was used to track endocytosed semiconductor quantum dots (QDs), yielding information on active transport of vesicular structures and passive diffusion within them.

The positional accuracy which can be achieved in lateral (x, y) and in axial (z) direction in regular imaging was estimated theoretically from the Cramer-Rao bound assuming a Gaussian-shaped intensity distribution of a single-molecule image.[12] The Cramer-Rao bound for the position and width of the Gaussian are given by $s_{\mu_x}^2 = s_{\mu_y}^2 = \sigma^2/(8N \ln 2)$ and $s_{\sigma^2}^2 = \sigma^4/N$ in which N is the total number of photons detected

by the camera and σ the full width at half maximum (FWHM) of the intensity distribution. By the change of the Gaussian width with focal distance the z position was calculated,[6]

$$z = \pm \frac{z_r}{\sigma_0} \sqrt{\sigma^2 - \sigma_0^2}, \quad (1)$$

in which z_r is the focal depth and σ_0 the diffraction-limited FWHM for a point source in focus. This dependence holds for $|z| < 2z_r \approx 1000$ nm. Error propagation finally leads to an axial accuracy $s_z^2 = 1/N((z_r^2/2z) + (z/2))^2$ in which the errors in z_r and σ_0 have been neglected. Both values were determined experimentally with high accuracy in independent experiments. Figures 1(a) and 1(b) (solid line) show both the lateral and the axial accuracies plotted versus the defocus position. Obviously the error in z around the focus is very large and negative and positive defocus cannot be distinguished given the symmetric dependence in z.

Introducing a weak cylindrical lens (f=10 m) into the emission beam path results in an axial astigmatism, γ, and hence provides an easy way to increase resolution in z.[11] The intensity distribution for a point emitter including astigmatism is described by

$$I(x,y) = N \frac{4 \ln 2}{\pi \sigma_r^2} \exp\left[-4 \ln 2 \left(\frac{(x - \mu_x)^2}{\sigma_r^2/\epsilon^2} + \frac{(y - \mu_y)^2}{\sigma_r^2 \epsilon^2} \right) \right], \quad (2)$$

in which the ellipticity $\epsilon = \sqrt{\sigma_y/\sigma_x}$ and a generalized width $\sigma_r^2 = \sqrt{\sigma_x^2 \sigma_y^2}$ were introduced. σ_x and σ_y are the FWHMs of the intensity distribution in x and y directions, respectively. Note that σ_x is not equal to σ_y except for one position in between the two foci, which we define as $z=0$ nm. By substituting z with $z+\gamma$ and $z-\gamma$ in Eq. (1) and using the definitions for σ_r and ϵ, the axial position is given by

$$z(\sigma_r, \epsilon) = \begin{cases} \dfrac{z_r}{\sigma_0} \sqrt{\dfrac{\sigma_r^2}{\epsilon^2} - \sigma_0^2} - \gamma, & \epsilon < 1 \\[2ex] -\dfrac{z_r}{\sigma_0} \sqrt{\sigma_r^2 \epsilon^2 - \sigma_0^2} + \gamma, & \epsilon > 1. \end{cases} \quad (3)$$

Analogous to the earlier treatment the Cramer-Rao bound leads to the accuracy in each direction:
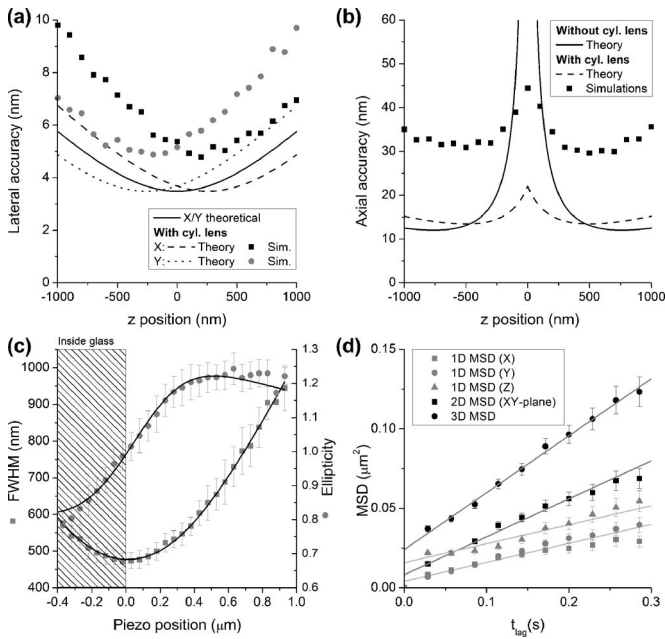
[a)]Electronic mail: schmidt@physics.leidenuniv.nl

FIG. 1. Positional accuracy in lateral (x,y) (a) and in axial (z) (b) direction for the detection of a fluorescing point object calculated according to the Cramer-Rao bound (lines) and compared to computer simulations (symbols). In the simulation each point object emitted an average of 4000 photons/frame. Each data point is an average of 1000 simulations. (c) σ_r and ϵ for QDs immobilized onto a glass substrate. Ten images containing nine QDs on average were taken per point. For $z<0$ the data deviate from the fit because the focal plane lies inside the coverslip. (d) MSD plots of diffusing QDs in a 15% dextran mixture (10 °C, frame rate=35 Hz).

$$s^2_{\mu_x} = \frac{1}{N}\frac{\sigma_r^2/\epsilon^2}{8\ln 2}, \quad s^2_{\mu_y} = \frac{1}{N}\frac{\sigma_r^2\epsilon^2}{8\ln 2}, \tag{4a}$$

$$s^2_z = \frac{1}{N}\left(\frac{\sqrt{5}z_r^2}{4(z\pm\gamma)} + \frac{\sqrt{5}}{4}(z\pm\gamma)\right)^2, \quad \epsilon \lessgtr 1. \tag{4b}$$

As shown in Figs. 1(a) and 1(b) the accuracy in z is largely increased compared to the case without cylinder lens while the accuracy in x and y is only slightly reduced.

The theoretical strategy described above was validated by simulations. Intensity profiles for fluorescing molecules were calculated as 2D Gaussians. Camera readout noise ($\sigma_r=23$ counts/pixel) and photon-counting statistics of the detector were fully taken into account. Additional background noise was neglected. The simulations, in which the signal-to-noise ratio (SNR) was varied from 20 to 1200, confirmed that the positional accuracy scaled with $\sqrt{N}$.[12] The positional accuracy obtained at a signal of 4000 photons/frame was 6 nm in lateral (x,y) and 30 nm in axial (z) direction [Figs. 1(a) and 1(b)]. It should be noted that the systematic deviation of the data from the predicted values is due to pixelation[12] which results in scaling factors of ~1.4 in lateral and ~2.1 in axial direction.

For calibration of the setup streptavidin-coated 705 nm QDs were spin coated onto a glass coverslip. QDs were excited for 20 ms at a laser intensity of 0.9 kW/cm^2 to obtain a SNR of 17 (275 photons/frame). σ_r and ϵ were measured while scanning the focal plane through the sample [Fig. 1(c)]. From these data the focal depth $z_r=474\pm4$ nm and the spot size $\sigma_0=443\pm1$ nm ($z=0$ nm) were determined from a fit to the given equations for σ_r and ϵ. The amount of astigmatism $\gamma=184$ nm equals that predicted. Compared to

the simulations the experimental results have an increased positional accuracy. We attribute this to an overestimation of z_r in the simulations leading to an underestimated increase of the width with defocus in the simulations. Typically 40 nm for the lateral directions (σ_x,σ_y) and 90 nm for the axial direction $(\sigma_z\approx 2.5\sigma_x)$ were achieved, confirming that the lateral accuracy is almost unchanged while axial accuracy is largely improved.

Subsequent to the calibration experiments, QDs were dissolved to a final concentration of 0.16 nM in 15% dextran T500. The viscosity of the solution ($\eta\approx 300$ cP at 10 °C) allowed us to follow the diffusional paths of the QDs for up to several minutes. From image sequences taken at a frequency of 35 Hz the 3D path was reconstructed. Each trajectory was analyzed in terms of the variation of the mean square displacement (MSD) with time delay between images. MSD analysis was performed for the full 3D positional information, for the projection of the trajectory onto the image plane (xy), and for the projection onto each of the three spatial directions x, y, and z [Fig. 1(d)], respectively. As predicted for free diffusion the MSD increases linearly with time according to $\mathrm{MSD}=2nDt+\Sigma 2\sigma_n^2$, characterized by the diffusion constant D of an n-dimensional process. The offset at zero time accounts for the positional accuracy in all three directions, $\sigma_{x,y}=47$ nm and $\sigma_z=90$ nm. Fit of the data to this model yielded $D=0.058\pm0.003$ μm^2/s, which is in excellent agreement with the free diffusion of a 22 nm diameter particle in a solution of viscosity $\eta=320$ cP following the Stokes-Einstein relation.

The methodology as characterized above was subsequently used to study intracellular transport processes. Human embryonic kidney cells [HEK293, see Fig. 2(a)] were incubated with a solution containing 0.1 nM QDs. The QDs were internalized within 2 h by endocytosis. A corresponding fluorescence image [Fig. 2(b)] showed several bright QDs that were easily identified in the low autofluorescence background of the cell. Trajectories for individual QDs were analyzed [Figs. 2(d) and 2(e)]. From the projections onto the 2D planes, the 3D trajectory clearly showed up. The QD in Fig. 2(d) displayed several mobility modes which were identified by analysis of the MSDs in parts of the trajectory [Figs. 2(f) and 2(g)]. In the initial part [Fig. 2(f)] the QD followed random diffusion ($D=0.015\pm0.001$ μm^2/s) in all dimensions. Subsequently [Fig. 2(g)] the QD followed a directed motion, as confirmed by a detailed analysis of the mobility in all three directions. The MSD increased supralinearly with lag time along the x and the z direction. Fitting the 3D-MSD (Ref. 13) yielded a velocity of $v=1.41\pm0.14$ μm/s for the QD's transport. Analysis of the movement perpendicular to the transport yielded diffusional behavior. In comparison, the QD shown in Fig. 2(e) was transported with lower velocity ($v=36\pm1$ nm/s). Perpendicular to the transport the mobility of the QD was confined[13] to a lateral confinement of side length $L=161\pm3$ nm. The size of the confinement was consistent with the typical size of endocytic vesicles. From this we interpret that QDs were actively transported inside vesicles presumably along cytoskeletal fibers. The typical transport velocities (1 μm/s) fell within the range characteristic for molecular motors in cells.[14]

In order to verify the contribution of active intracellular transport to the observed movements, cells already containing QDs were depleted from ATP by an incubation with 20 mM NaN$_3$ and 12 mM 2-deoxy-D-glucose for 1 h. After
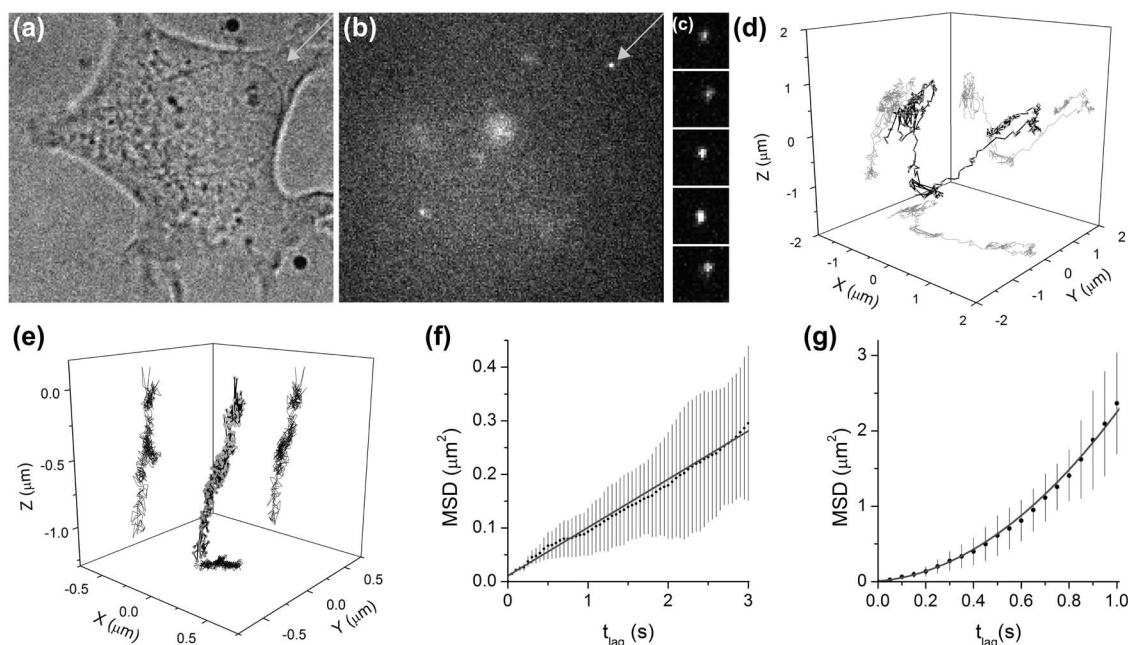
FIG. 2. HEK293 cell loaded with QDs by endocytosis. (a) Transmission image of the cell (image: 48×42 μm). (b) Fluorescence image of the same cell (exposure time=6 ms, signal=670 photons/frame). (c) Five consecutive images of a QD inside the cell [indicated by the arrow in (a) and (b)] taken at a delay of 50 ms [images: $(4 \ \mu$m$)^2$]. The change in ellipticity can be clearly seen. [(d) and (e)] 3D trajectories of different QDs tracked during 500 image frames. [(f) and (g)] 3D-MSD of different parts of the trajectory in (d).

incubation directed movement [Figs. 2(d) and 2(e)] was abolished while random diffusion was still observed (data not shown). Hence, the supralinear dependence of MSD with time was attributed to ATP dependent intracellular processes.

In conclusion, the introduction of a slight astigmatism into the optical system of a microscope allowed us to extend the positional detection of individual QDs in life-cell imaging to the full 3D volume. For QDs the positional accuracies achieved approached the theoretical limit set by the Cramer-Rao bound and were 43 nm in lateral and 130 nm in axial direction inside cells at a frame rate of 167 Hz. The power of the methodology was demonstrated by detailed analysis of the motion of individual QDs endocytosed by cells. The additional abilities of the 3D approach was most obviously demonstrated in Fig. 2. While a conventional 2D approach would only have shown free diffusion and transport in a plane, the 3D trajectory shows that the QD was transported along a tubular structure that extended into the third dimension. Hence, a 2D approach would have resulted in an incomplete interpretation of the observations.

In extrapolation of the results the fast 3D tracking of individual fluorescent proteins such as the green fluorescent protein, however, seems exceedingly difficult. Typically in those experiments 150 photons/frame are detected from a single molecule which would lead to an axial accuracy of $\sigma_z = 120$ nm at optimal background conditions. Better results will be achieved for multiple-labeled $(5 \times -10 \times)$ objects. This will yield longer trajectories and signals of 4000 photons/frame and higher, in particular, when additionally the excitation intensity is increased. In this way dynamic localization of, e.g., vesicles inside cells, at resolutions of 6 nm in lateral and 30 nm in axial direction can be easily obtained. Hence, the application of this fast life-cell imaging methodology to the study of, e.g., vesicle trafficking or virus entry,[15,16] will prove highly valuable and might help to lift ambiguities in present models of cellular transport.

[1] G. S. Harms, L. Cognet, P. H. M. Lommerse, G. A. Blab, H. Kahr, R. Gamsjager, H. P. Spaink, N. M. Soldatov, C. Romanin, and T. Schmidt, Biophys. J. **81**, 2639 (2001).

[2] M. Vrljic, S. Y. Nishimura, S. Brasselet, W. E. Moerner, and H. M. McConnell, Biophys. J. **83**, 2681 (2002).

[3] M. Dahan, S. Levi, C. Luccardini, P. Rostaing, B. Riveau, and A. Triller, Science **302**, 442 (2003).

[4] C. Tardin, L. Cognet, C. Bats, B. Lounis, and D. Choquet, EMBO J. **22**, 4656 (2003).

[5] J. Gelles, B. J. Schnapp, and M. P. Sheetz, Nature (London) **331**, 450 (1988).

[6] G. J. Schütz, V. P. Pastushenko, H. J. Gruber, H.-G. Knaus, B. Pragl, and H. Schindler, Single Mol. **1**, 25 (2000).

[7] A. M. van Oijen, J. Köhler, J. Schmidt, M. Müller, and G. J. Brakenhoff, Chem. Phys. Lett. **292**, 183 (1998).

[8] M. Speidel, A. Jonas, and E. L. Florin, Opt. Lett. **28**, 69 (2003).

[9] V. Levi, Q. Q. Ruan, and E. Gratton, Biophys. J. **88**, 2919 (2005).

[10] T. Schmidt, G. J. Schütz, W. Baumgartner, H. J. Gruber, and H. Schindler, Proc. Natl. Acad. Sci. U.S.A. **93**, 2926 (1996).

[11] H. P. Kao and A. S. Verkman, Biophys. J. **67**, 1291 (1994).

[12] R. J. Ober, S. Ram, and E. S. Ward, Biophys. J. **86**, 1185 (2004).

[13] M. J. Saxton and K. Jacobson, Annu. Rev. Biophys. Biomol. Struct. **26**, 373 (1997).

[14] X. L. Nan, P. A. Sims, P. Chen, and X. S. Xie, J. Phys. Chem. B **109**, 24220 (2005).

[15] G. Seisenberger, M. U. Ried, T. Endress, H. Büning, M. Hallek, and C. Bräuchle, Science **294**, 1929 (2001).

[16] H. P. Babcock, C. Chen, and X. W. Zhuang, Annu. Rev. Biophys. Biomol. Struct. **87**, 2749 (2004).